In Situ Measurements of Thermal Ion Temperature in the Martian Ionosphere

K. G. Hanley[1] [ID]**, J. P. McFadden[1]** [ID]**, D. L. Mitchell[1]** [ID]**, C. M. Fowler[1,2]** [ID]**, S. W. Stone[3]** [ID]**, R. V. Yelle[3]** [ID]**, M. Mayyasi[4]** [ID]**, R. E. Ergun[5]** [ID]**, L. Andersson[5]** [ID]**, M. Benna[6,7], M. K. Elrod[6,8]** [ID]**, and B. M. Jakosky[5]** [ID]

[1]Space Sciences Laboratory, University of California Berkeley, Berkeley, CA, USA, [2]Department of Physics and Astronomy, West Virginia University, Morgantown, WV, USA, [3]Lunar and Planetary Laboratory, University of Arizona, Tucson, AZ, USA, [4]Astronomy Department, Boston University, Boston, MA, USA, [5]Laboratory for Atmospheric and Space Physics, University of Colorado Boulder, Boulder, CO, USA, [6]Center for Research and Exploration in Space Science and Technology, NASA Goddard Space Flight Center, Greenbelt, MD, USA, [7]University of Maryland, Baltimore County, MD, USA, [8]University of Maryland, College Park, MD, USA

Abstract In situ measurements of ionospheric and thermospheric temperatures are experimentally challenging because orbiting spacecraft typically travel supersonically with respect to the cold gas and plasma. We present O_2^+ temperatures in Mars' ionosphere derived from data measured by the SupraThermal And Thermal Ion Composition instrument onboard the Mars Atmosphere and Volatile EvolutioN spacecraft. We focus on data obtained during nine special orbit maneuvers known as Deep Dips, during which MAVEN lowered its periapsis altitude from the nominal 150 to 120 km for 1 week in order to sample the ionospheric main peak and approach the homopause. We use two independent techniques to calculate ion temperatures from the measured energy and angular widths of the supersonic ram ion beam. After correcting for background and instrument response, we are able to measure ion temperatures as low as 100 K with associated uncertainties as low as 10%. It is theoretically expected that ion temperatures will converge to the neutral temperature at altitudes below the exobase region (∼180–200 km) due to strong collisional coupling; however, no evidence of the expected thermalization is observed. We have eliminated several possible explanations for the observed temperature difference between ions and neutrals, including Coulomb collisions with electrons, Joule heating, and heating caused by interactions with the spacecraft. The source of the energy maintaining the high ion temperatures remains unclear, suggesting that a fundamental piece of physics is missing from existing models of the Martian ionosphere.

Plain Language Summary A small fraction of a planet's atmosphere, the ionosphere, exists as a plasma made of positive ions produced when sunlight removes an electron from a neutral particle. We measured the temperatures of ions in Mars' lower ionosphere for the first time since 1976 using an instrument called SupraThermal And Thermal Ion Composition on the Mars Atmosphere and Volatile EvolutioN spacecraft. In the part of the ionosphere with the most ions, ions were expected to have the same temperature as the neutral atmosphere because ions and neutrals collide with each other many times per second. However, we found that during the day, the ions were more than 100 K hotter than the neutrals. We eliminated many possible sources of energy for the ions, including sunlight, collisions with electrons, chemical reactions, and electric fields in Mars' atmosphere. The source of the energy that keeps the ions hot remains unclear, suggesting that a fundamental piece of physics is missing from existing models of the Martian ionosphere.

1. Introduction

Ion temperature is an important parameter that influences the structure and evolution of atmospheres (Schunk & Nagy, 2009). Ion temperatures affect collision and chemical reaction rates, so precise knowledge of ion temperatures and the chemical processes operating in planetary atmospheres enables a more thorough understanding of composition and structure in the photochemical region (Fox, 2015). Ion temperatures also influence atmospheric dynamics and energetics. Specifically, hotter temperatures allow more ions to overcome gravity and reach altitudes above the exobase, where electromagnetic forces can accelerate ions to escape velocity. Understanding how ions are supplied to the exosphere is important for a complete description of ion escape during the present epoch (Chassefière & Leblanc, 2004), and can illuminate how ion loss might have varied under different conditions at

earlier times. At Mars, ion escape to space is believed to be one of the major mechanisms through which the once Earth-like (i.e., 0.1–1 bar) atmosphere was lost (Jakosky et al., 2018), and escape of hot O through the dissociative recombination of O_2^+ dominates atmospheric loss in the present epoch (Jakosky et al., 2018; McElroy, 1972). Measurements of ion temperature are necessary in order to investigate the poorly understood supply of planetary ions to the exosphere, their acceleration to higher altitudes, and the critical role that ion temperature is likely to have played in the climate evolution of the planet.

At Mars, ion temperature measurements thus far have been limited. The first measurements were made by retarding potential analyzers (RPAs) during the descents of the two Viking landers in 1976 (Hanson et al., 1977). These measurements relied on fits of overlapping signals, and are sensitive to assumptions made about the relative abundances of different ions. Additionally, RPAs are sensitive to total current, and thus only provide a 1-D measurement. Subsequent measurements of 3-D ion temperature moments were provided by the ASPERA-3 instrument onboard Mars Express (Barabash et al., 2006). ASPERA-3 measurements are limited to altitudes above 300 km, too high to sample the cold ionospheric populations observed by Viking and in a regime where the spacecraft speed is usually smaller than the ions' thermal speed. Measuring colder ion temperatures at lower altitudes, where spacecraft velocities are larger than ion thermal velocities, is more complex and requires careful consideration of instrumental effects.

The basic structure of Mars' dayside ionosphere is well understood. Comprehensive reviews of the dayside ionosphere are available in Schunk and Nagy (2009), Withers (2009), and Haider et al. (2011). The dayside ionosphere is primarily a result of ionization and dissociation of atmospheric CO_2 by sunlight. The CO_2^+ is quickly converted to O_2^+ through chemical reactions, making O_2^+ the dominant ion. Since the ionosphere is dominated by a single species, the variation of ion density with altitude and solar zenith angle (SZA) is well-described by a Chapman function at low altitudes, with the ionospheric peak typically occurring near altitudes of 120 km at the sub-solar point and increasing to ~180 km near the terminator (Ergun et al., 2015; Fallows et al., 2015a, 2015b; González-Galindo et al., 2021). On the nightside, major sources of plasma include electron impact ionization and transport from the dayside (Adams et al., 2018; Fowler et al., 2015; Fox et al., 1993; Girazian et al., 2017; Lillis et al., 2011), which is a function of ion temperature.

The vast majority of investigations of ion temperatures at Mars have relied on models which attempt to reproduce the two Viking descent profiles. Some of the first models created after the Viking missions (e.g., Chen et al., 1978; Fox & Dalgarno, 1979; Rohrbaugh et al., 1979) used Viking measurements as inputs to investigate the composition and structure of the ionosphere; Rohrbaugh et al. (1979) showed that accounting for the heat released during atmospheric chemical reactions was important for reproducing Viking profiles. Since Viking, many new types of models have been developed and used to study the Mars system. While each model includes different physics, many of the underlying assumptions are the same. Below the exobase (~170–200 km), where the mean free path of a particle is shorter than its scale height, theory suggests that high collision rates will force ions, neutrals, and electrons to equilibrate. Most models (e.g., Andersson et al., 2010; Bougher et al., 2015; C. Dong et al., 2014; Ma et al., 2019; Matta et al., 2014) assume that ion and neutral temperatures converge a few scale heights ($\frac{kT_n}{m_n g} \sim 11$ km) below the exobase region, with the electron temperature converging at some lower altitude. At higher altitudes, the ion temperature is either estimated from the neutral and electron temperatures (e.g., Bougher et al., 2015; C. Dong et al., 2014), or calculated from kinetic or fluid approximations, often including some heat source from above the ionosphere (e.g., plasma waves) to improve agreement with Viking observations (e.g., Andersson et al., 2010; Ma et al., 2019; Matta et al., 2014).

In this paper, we present the first measurements of thermal ion temperatures at Mars since the Viking RPAs. The Mars Atmosphere and Volatile EvolutioN (MAVEN) spacecraft has been in a 75° inclination elliptical orbit, with a typical periapsis altitude of ~150 km, since late 2014 (Jakosky et al., 2015). Orbit precession allows periapsis to sample all local times and latitudes from 75°S to 75°N. To date, the orbit has made seven revolutions in local time over a span of 3.3 Mars years. During nine one-week periods called Deep Dips (DDs), MAVEN lowered its periapsis to ~120 km, which approaches the top of the well-mixed lower atmosphere and samples the ionospheric main peak. In this study, we have used data collected by the SupraThermal And Thermal Ion Composition (STATIC) instrument to calculate O_2^+ temperatures for more than 150 MAVEN orbits spanning DDs 5–9. These new ion temperature measurements provide important new constraints on ionospheric chemistry and structure.
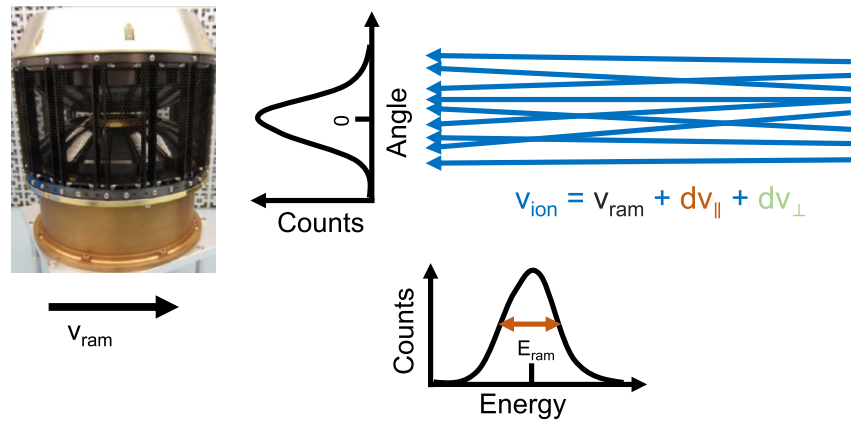
Figure 1. This schematic illustrates how STATIC measures the temperature of a cold ion beam while traveling supersonically. In the frame of the instrument, which has a spacecraft potential of V_{sc}, ions with charge q enter from the ram direction with energy $E_{beam} = \frac{1}{2}mv_{ram}^2 - qV_{sc}$. The variance of the velocity distribution function around the beam velocity provides a measurement of the temperature. Deviations in the velocity component parallel (perpendicular) to the ram direction are measured using the energy (angular) beamwidth from the c6 (c8) data product.

2. Methods

The STATIC instrument is a toroidal top-hat electrostatic analyzer with electrostatic deflectors and a time-of-flight analyzer (McFadden et al., 2015), located at the end of a 2-m boom on MAVEN's Articulated Payload Platform. Ions within a selected energy band pass through the analyzer and enter the time-of-flight section. By sweeping the analyzer and deflector voltages in a 4-second cycle, STATIC measures ions in 64 energy bins ranging from 0.1 eV to 30 keV over a 360°x90° field of view with mass resolution capable of distinguishing the main ionospheric and escaping species: CO_2^+, O_2^+, O^+, and H^+. To increase its dynamic range, STATIC is equipped with both a mechanical attenuator, which reduces ram fluxes by a factor of 100, and an electrostatic attenuator, which reduces fluxes by a factor of 10 across the entire field of view. Each attenuator can be activated independently. The five-dimensional (time, energy, azimuthal angle, polar angle, and mass) distribution functions are summed and possibly downsampled over one or more of the five dimensions, creating lower-resolution data products to reduce the amount of data that must be stored and transmitted to Earth. For most data products, pairs of adjacent energy bins are summed to reduce the number of energy bins to 32 or less.

We use two different data products, "c6" and "c8," to make two independent calculations of O_2^+ temperatures for each measured distribution. The c6 data product is summed over both angles to produce a distribution with 32 energy channels and 64 mass channels. We refer to the measurement based on the c6 data product, which calculates temperature based on ion velocity along the ram direction (Figure 1), as the "energy beamwidth." The c8 data product is summed over mass and instrument azimuth to produce a distribution of 32 energies and 16 deflection angles. At low altitudes, the ionosphere is dominated by a single species (O_2^+) and the instrument is oriented such that the deflection angle is orthogonal to the ram direction. This allows for a measurement of temperature based on velocity perpendicular to the ram direction, using the electrostatic deflectors. The temperature measurement based on c8 data is referred to as the "angular beamwidth." Background subtraction is performed separately for each data product and will be described in detail in a forthcoming publication.

Plasma temperature is usually calculated by integrating the second moment of a measured velocity distribution function $f_M(\vec{v})$ across the field of view of the instrument, and dividing by the zeroth order moment, the density n:

$$T = \frac{1}{n} \int m(\vec{v} - \vec{v}_{bulk})^2 f_M(v, \theta, \phi) v^2 \sin\theta \, dv \, d\theta \, d\phi \tag{1}$$

where m is the ion mass, $\vec{v}$ is the total ion velocity, and $\vec{v}_{bulk}$ is the bulk flow velocity in the spacecraft frame. Equation 1 is valid if ion thermal velocities are greater than the spacecraft velocity because ions can enter the analyzer from any part of the field of view. However, for a spacecraft traveling much faster than the ion thermal velocity, as is the case for MAVEN periapsis passes, accurate determination of the ion temperature is more difficult. In this scenario, ions enter the analyzer as a beam centered on the single anode which faces into the ram

direction. Integrating the measured distribution function over the instrument field of view using Equation 1 will yield an inaccurate result since typical beamwidths of 6° are much smaller than the anode resolution (22.5°). If the instrument is oriented as depicted in Figure 1, the temperature can still be accurately determined by calculating the variance of the distribution as a function of velocity parallel or perpendicular to the instrument. Both temperature measurement methods rely on the assumption that the measured distribution is beam-like, that is, the spacecraft travels supersonically so that thermal velocities are much less than the ram velocity (Figure 1). For omnidirectional c6 data, a beam is defined as a distribution in which 75% of the counts are measured in a certain number of energy bins surrounding the bin with the most counts after background subtraction, with the number of bins used depending on the instrument's energy and angular resolution. The threshold of 75% was chosen empirically to minimize data gaps while making sure derived temperatures are physically meaningful (see Section 3, paragraph 5).

An example of STATIC c6 and c8 data collected during a periapsis pass during a Deep Dip is shown in Figures 2a and 2b. Gaps in the energy flux in Figures 2a and 2b occur when the geometric factor changes during a measurement due to a change in mode or attenuator state. There are more data gaps in the c8 data due to how the onboard Data Processing Unit operates. If the velocity distribution function $f(v)$ is Maxwellian, the variance σ^2 of the measured distribution $f_M(v)$ is related to the temperature:

$$\sigma^2 = \int (v - v_{\text{bulk}})^2 f_M(v) \mathrm{d}v = \frac{k_B (T_{\text{ion}} + T_{\text{AC}})}{m} \tag{2}$$

where k_B is Boltzmann's constant; T_{ion} is the temperature of the ion distribution; T_{AC} is an analyzer correction due to a combination of instrumental effects; and v is the velocity parallel (perpendicular) to the ram direction for the energy (angular) beamwidth, corrected for spacecraft potential. The analyzer correction term appears because the measured distribution function $f_M(v)$ is a convolution of the actual distribution $f(v)$ and the analyzer response function $g(v)$, which can both be approximated by gaussians:

$$f_M(v) \sim (f * g)(v) \sim \int \exp \frac{-(v' - v_{\text{bulk}})^2}{2\sigma_f^2} \exp \frac{-(v' - v)^2}{2\sigma_g^2} \mathrm{d}v' \tag{3}$$

where $\sigma_f^2 = \frac{k_B T_{\text{ion}}}{m}, \sigma_g^2 = \frac{k_B T_{\text{AC}}}{m}$, and we have omitted the prefactors that determine the units. Since the convolution of two gaussians is a gaussian with a width equal to the sum of their individual widths, the finite contribution to σ^2 from instrumental broadening can just be subtracted off. When the distribution is broad enough that Equation 1 is valid (i.e., $T_{\text{ion}} \gg T_{\text{AC}}$), the instrument response can be ignored.

The conversion of count rate to $f_M(v)$ requires knowledge of spacecraft potential. Spacecraft potential is estimated from the STATIC data at 4 s cadence. At low altitudes (<180 km), potentials are estimated from the difference between the expected O_2^+ ram energy and the measured beam energy. At higher altitudes (>300 km), potentials are estimated from the minimum energy at which protons are observed. Between 180 and 300 km, the lower of the two potential estimates is used, with some qualifications on count rates. In addition, this estimate is modified to account for the effect of changes in spacecraft potential produced by current-voltage (IV) sweeps conducted by MAVEN's Langmuir Probe and Waves (LPW) experiment (Ergun et al., 2015) during each 4 s ion measurement.

The analyzer correction is calculated and subtracted for each measured distribution through a process described in Section 2.1. The energy and angular beamwidth temperatures generally agree very well through periapsis (Figure 2c). Differences can result from the presence of a significant suprathermal population, rapid changes in spacecraft potential during a measurement, a change in beam velocity due to a change in winds (generally negligible) during a measurement, errors in the corrections for non-ideal analyzer response, errors in background subtraction, and statistical fluctuations. The uncertainties associated with each measurement method are shown in Figure 2d. Once the temperature has been calculated, the assumption of a Maxwell-Boltzmann distribution can be verified with a model (Figures 2e and 2f).

An algorithm was developed to (a) determine if each temperature calculation is likely to be valid and (b) select the most reliable of the two values (energy or angular beamwidth). Measurements can be invalidated if the count rate is too low; if $T_{\text{AC}} > 2T_{\text{ion}}$; if the spacecraft potential is unknown or is <−3.5 V; or if the peak of the distribution lies outside the field of view. The measurement with the smallest T_{AC}, usually the energy beamwidth, is considered to be most reliable. In regions where the algorithm might switch back and forth between data products
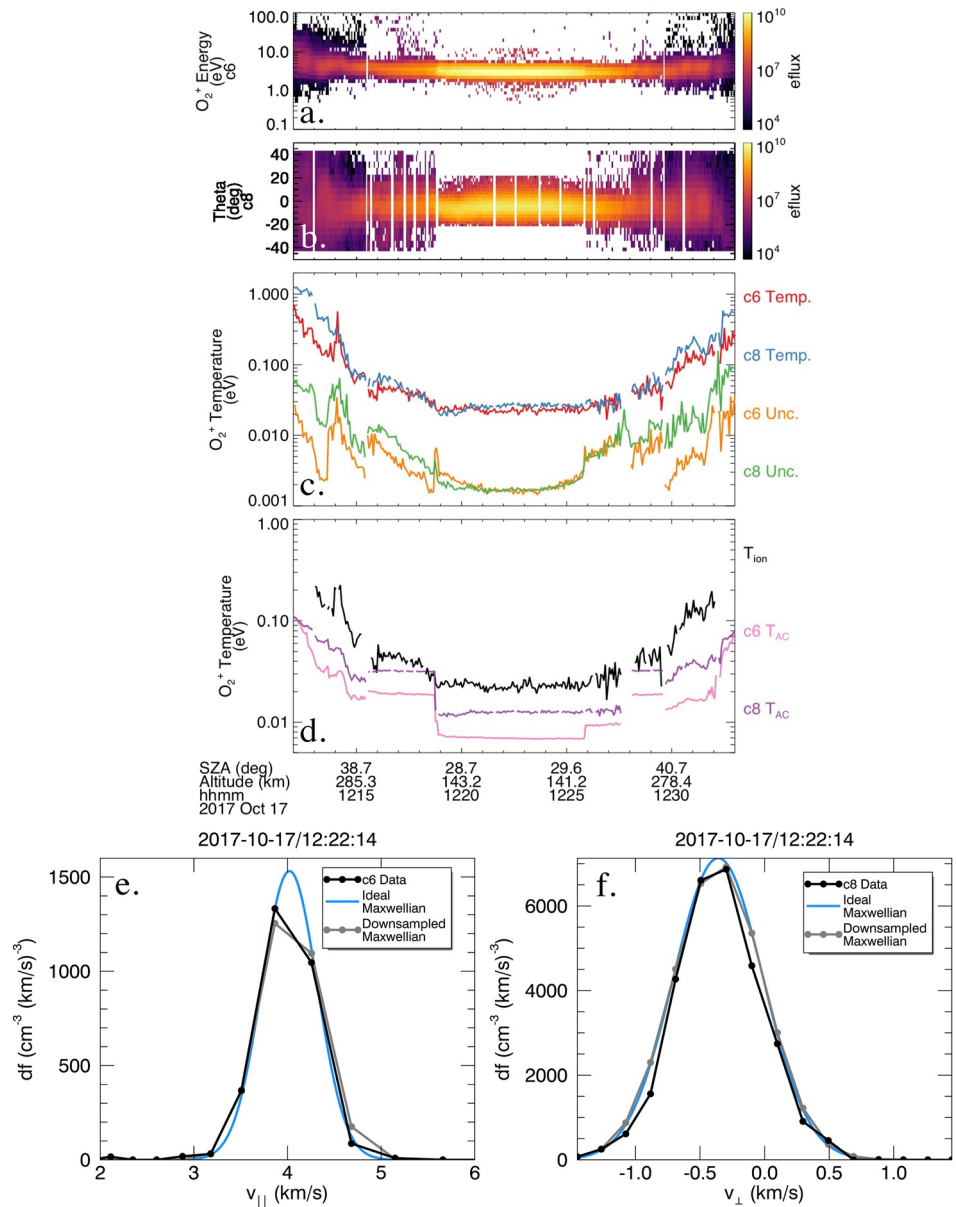
Figure 2. Panel (a) c6 energy spectrogram for O_2^+ during one periapsis pass. Energy flux has units of eV/cm^2/s/steradian/eV. Panel (b) c8 deflector angle distribution. Panel (c) Measured O_2^+ energy (angular) beamwidth temperatures in red (blue), and associated statistical uncertainties in orange (green). Panel (d) Final O_2^+ temperature in black and analyzer corrections for the energy and angular beamwidths in pink and purple. Discontinuities in T_{AC} correspond to changes in mode and attenuator state, which impact instrument resolution. Solar zenith angle and altitude are indicated at the bottom of the plot. Panel (e) A c6 distribution function, not corrected for spacecraft motion. The blue line is not fitted to the data, but represents an ideal Maxwell-Boltzmann distribution with the same temperature and bulk velocity as the measured distribution. The peak of the measured distribution function is used as a scaling factor. The ideal Maxwellian is downsampled by averaging over each STATIC energy bin to produce the gray points. Panel (f) A c8 distribution function. The blue and gray Maxwellians are produced using the same process as panel (e). The magnitudes of the distribution functions differ due to assumptions made about the angular coverage of the distribution for c6 data.

at adjacent timestamps, potentially introducing false temperature fluctuations into the profiles, a second round of processing forces the algorithm to choose one method. Secondary processing is necessary on orbits where both calculations require larger corrections, such as orbits with highly negative spacecraft potential. For the majority of MAVEN periapsis passes, including the DD passes described here, the errors are small and do not significantly impact the results.

2.1. Removal of Systematic Errors

Before the temperature is calculated, the data are first corrected for an instrument effect known as "ion suppression." As different parts of the sensor are exposed to different fluxes of atomic oxygen at different altitudes and SZAs, internal analyzer surfaces experience small changes in surface potential (contact potential or work function) due to chemical changes from exposure. These non-uniform changes have resulted in a time-varying detuning of the electrostatic analyzer. However, the effect of this detuning, other than reducing analyzer sensitivity (i.e., height of the distribution function), has an almost negligible impact on measured temperature (i.e., width of the distribution function). We include it primarily to rule out its influence on our measurements. By August 2015, sensitivity returned to a level that allowed reliable corrections for the sensitivity reduction to be applied for energies > 3 eV. We only use data collected after September 2015 in this analysis.

The analyzer correction T_{AC} is calculated independently for the energy and angle beamwidths and consists of two empirically derived terms: (a) $T_{response}$, a correction for the finite energy and angular resolution of the instrument and (b) $T_{scatter}$, a scattering term which is activated when the O_2^+ ram energy (after passing through the spacecraft potential) is > 4 eV. We will now explain the origin and form of each term in T_{AC}.

The analyzer response term corrects for the broadening introduced by the instrument's finite energy and angular resolution. Even if STATIC sampled a perfectly monoenergetic beam, the beam would appear to have some finite width due to the finite analyzer response as seen in Figures 12 and 13 of McFadden et al. (2015). Additional broadening (i.e., smearing out in energy) is introduced by the onboard summing of adjacent energy bins described in Section 2. For any electrostatic analyzer with a high-voltage power supply, any ripple in the power supply will also introduce broadening, although this effect has not been observed for STATIC. Each of these effects can be removed using a term of the form:

$$T_{response} = \frac{\Delta E}{E} E_c \tag{4}$$

in which $T_{response}$ is given in eV, $\frac{\Delta E}{E}$ is the empirically determined analyzer response, and E_c is the characteristic energy obtained by dividing the beam's energy flux by its flux. This form results from the analyzer having an energy acceptance ΔE which is proportional to E, and from the use of a logarithmic energy sweep.

A scattering term was included in T_{AC} because energy dependent ion backscattering is observed by STATIC. At periapsis, ions that are scattered off the entrance aperture posts are sometimes detected entering the analyzer from the anti-ram direction. These ions are not observed when the spacecraft potential is near zero and the O_2^+ beam energy is ∼3 eV. However, for spacecraft potentials <−1 V and O_2^+ energies >4 eV, these backscattered ions are observed with increasing relative flux with ion energy. These backscattered ions are eliminated in our temperature analysis. However, the same scattering processes are expected to happen on surfaces internal to the analyzer, resulting in an effective energy broadening. This energy broadening from scattering was first detected through changes in measured temperature associated with an observational procedure that caused spacecraft potential to change by 2 V on adjacent orbits. The broadening due to scattering was only observed when the O_2^+ beam energy was > 4 eV, and the effective change in resolution was observed to plateau at higher energies. A search of the literature did not reveal any theory or measurements that describe scattering of low energy ions off surfaces (most low energy ions charge exchange to become neutrals). We therefore developed an empirical formula with the observed characteristics to correct for the scattering. The formula was verified using observational procedures that shifted the O_2^+ beam energy on adjacent orbits, so that temperatures measured under similar environmental conditions could be compared. The verification procedure will be described in detail in Section 2.3.

Broadening due to internal scattering was removed using a correction of the form:

$$T_{scatter} = \begin{cases} 0 & \text{if } E_c < E_{scatter} \\ S_1 E_c \left(\frac{(E_c - E_{scatter})}{E_{scatter}} \right)^{S_2} & \text{if } E_{scatter} \leq E_c < (E_{scatter} + \Delta E_{scatter}) \\ S_1 E_c \left(\frac{(E_{scatter} + \Delta E_{scatter})}{E_{scatter}} \right)^{S_2} & \text{if } E_c \geq (E_{scatter} + \Delta E_{scatter}) \end{cases} \tag{5}$$

Table 1
STATIC Analyzer Correction Constants

Parameter	Energy value	Angular value
$E_{scatter}$	4.0	4.0
$\Delta E_{scatter}$	2.0	2.0
S_1	0.0065	0.0025
S_2	0.8	0.8

in which $E_{scatter}$ is the lowest energy at which scattering is observed and $E_{scatter} + \Delta E_{scatter}$ is the energy at which the broadening due to scattering stops increasing. The values of $E_{scatter}$, $\Delta E_{scatter}$, S_1, and S_2 were determined empirically, and they differ for the energy and angular beamwidths (Table 1). Note that $T_{scatter}$ is zero for Deep Dip orbits, where the spacecraft potential is close to zero.

The forms and constants used for each term in T_{AC} were verified independently of one another. The procedures used to validate each correction will be described in Section 2.3.

The last known source of systematic error is variation in the spacecraft potential during the STATIC measurement of a cold ion beam. According to Liouville's theorem, the distribution function is corrected for spacecraft potential by simply adding the spacecraft potential to the measured ion energy, shifting the distribution function to lower energies for negative spacecraft potentials. However, the IV sweeps conducted by LPW can cause the spacecraft potential to change significantly (by tenths of a Volt) during the portion of STATIC's energy sweep when the ion beam is measured. Fortunately, LPW monitors these changes with sufficiently high time resolution so that the spacecraft potential can be calculated separately during each STATIC energy step. Without this correction, ion energies are shifted by the wrong spacecraft potential, which significantly alters the shape of the distribution function.

2.2. Sources of Uncertainty

Sources of uncertainty in STATIC ion temperature measurements include random errors from statistical fluctuations, uncertainty in the spacecraft potential, and unidentified systematic errors in estimated T_{AC}, which are expected to be negligible. We have employed a set of rigorous processes to identify, correct, and validate sources of uncertainty in derived ion temperatures, which are described in detail in Section 2.3. Our validation techniques suggest that uncertainties are small and derived ion temperatures are accurate.

The uncertainty introduced into each measurement by statistical fluctuations is plotted in Figure 2c. Poisson theory states that the uncertainty in the number of counts in a bin is given by the square root of the number of counts, N, which is assumed to be known exactly. However, for measurements obtained by spacecraft, N is measured only once and is subject to statistical fluctuations. Taking the statistical uncertainty to be the square root of $N_{measured}$ can therefore over- or underestimate the uncertainty in the temperature by as much as 35%, with larger effects for smaller values of N. To ensure accurate calculation of the statistical uncertainty, we simulate repeated measurements of each distribution with random noise added, until N for the peak bin stops changing. The statistical uncertainty is then propagated in the usual way.

We examined the results of artificially changing the measured spacecraft potential on the temperature measurements, since uncertainty in the absolute spacecraft potential could be one of the biggest sources of uncertainty in our measurements. As we expected, the analyzer response correction $T_{response}$, which corrects for the different resolution of the instrument at different energies, causes the final measured temperature to shift by a small amount linearly, which should be negligible for nominal uncertainties of calculated potential.

2.3. Validation

Although no external data set exists that covers all the conditions sampled by STATIC, the large volume of data collected by STATIC makes validation possible. The most compelling evidence that all systematic errors have been removed from STATIC data is the agreement between the two independent measurements of the O_2^+ temperature. The energy and angular beamwidths generally agree within 10% (Figure 2c), and any significant discrepancies between them can often be explained on a case-by-case basis.

The terms in the temperature correction T_{AC} were calculated independently using empirical methods and ground calibrations. These corrections have been validated via investigation of hundreds of orbits spanning a range of conditions that are known to influence T_{AC}, including spacecraft orientation, instrument mode, attenuator state, and SZA. These orbits also sampled many different geographic locations, Mars seasons, and solar conditions in

order to verify that accurate, continuous temperature profiles are produced regardless of environmental conditions. We will now describe how each term in T_{AC} was independently verified.

The analyzer response term $T_{response}$ varies with instrument mode and attenuator state. STATIC's energy and deflector sweeps sample different energy and angular ranges depending on instrument mode, but the 4-second sweep time is constant. The energy and angular resolutions are therefore different in different modes and require different corrections. Additionally, the energy-angle response differs if ions can enter across the entire field of view, or are restricted to the edges by the attenuators. The form and constants used to calculate $T_{response}$ were determined from analyzer design simulations and ground calibrations (McFadden et al., 2015), and then slightly adjusted to eliminate discontinuities in temperature profiles which coincide with changes in instrument mode and attenuator state.

The analyzer response correction was also verified using a simulation. Maxwellian distribution functions of known temperature, density, and drift velocity were generated and sampled using a simulated version of STATIC. We used the empirically derived analyzer response functions to introduce instrument broadening, measured the temperature as described above, then applied the analyzer broadening correction $T_{response}$. A random number generator was used to account for the effects of statistical fluctuations. The simulation was repeated for all combinations of activation states of the mechanical and electrostatic attenuators; the results are shown in Figure 3. Above 100 K, the analyzer broadening is successfully corrected. Residual errors average around 5% for ion temperatures of 100 K and grow significantly for colder temperatures. Measurements of corrected temperature below 60 K, where the corrected temperature levels off in Figure 3e, are removed from the data set.

The scattering term $T_{scatter}$ is a function of spacecraft potential, which can be intentionally varied by flying the spacecraft in different orientations. Since large (i.e., order-of-magnitude) changes in temperatures below the exobase region are not expected between adjacent orbits, corrections based on the spacecraft potential can be tested by varying the attitude of the spacecraft on adjacent orbits and comparing the measured temperature profiles. Specifically, the spacecraft is oriented so that ram flow impacts the solar panels edge-on ("Fly-Y") or face-on ("Fly-Z"). In Fly-Y, the ram ion current is collected by the side of the spacecraft bus facing the flow and by the "gull-wing" outer segment of the leading solar panel with its conducting back face at an 80° angle to the flow. In this configuration, the total ion current is somewhat less than the electron current, so the spacecraft charges a few Volts negative to repel some of the electrons and achieve zero net current. However, in Fly-Z, the broad faces of the backs of the solar panels collect enough ion current to cancel the electron current, so the spacecraft potential is close to zero. A representative value for spacecraft potential at periapsis in Fly-Z is −0.12 V, while the spacecraft potential ranges from −1 to −4 V at periapsis in Fly-Y. We have conducted six "Alternating Fly-Y Fly-Z Campaigns" of 11–15 orbits each in order to verify the scattering correction. MAVEN is always oriented in Fly-Z during DDs.

Finally, we can compare profiles measured by STATIC to the profiles measured by the Viking RPAs (Figure 4). Viking 1 landed at 16:00 local time, near the Northern summer solstice with a solar longitude $L_S = 97°$ and Viking 2 landed at 10:00, $L_S = 117°$. MAVEN's orbital configuration is closest to the Viking lander trajectories during DD 8 for which periapsis occurred at 14:00 and $L_S = 76°$. At altitudes above the exobase, agreement between STATIC and both Vikings is good. At lower altitudes, both Vikings measured substantially colder temperatures than STATIC observed during DD 8. The difference in Viking profiles and DD 8 profiles cannot be explained by solar activity: we estimate solar Lyman-alpha fluxes at Mars of 2.2×10^{-3} W/m^2 and 2.4×10^{-3} W/m^2 for Viking 1 and 2, and 2.2×10^{-3} W/m^2 for DD 8. Values of composite solar Lyman-alpha fluxes were taken from the LASP Interactive Solar Irradiance Datacenter and extrapolated to Mars using the method described in Thiemann et al. (2017). It is important to note that at different local times, STATIC can and does observe temperatures as cold as those measured by the Viking landers. The median temperature profile measured during DD 6, which occurred at 01:00 and $L_S = 194°$, is included in Figure 4 to illustrate the large variety of temperatures measured by STATIC at different locations.

The measurements and discussion presented here indicate that the corrections needed to calculate ion temperatures from STATIC data are well understood.
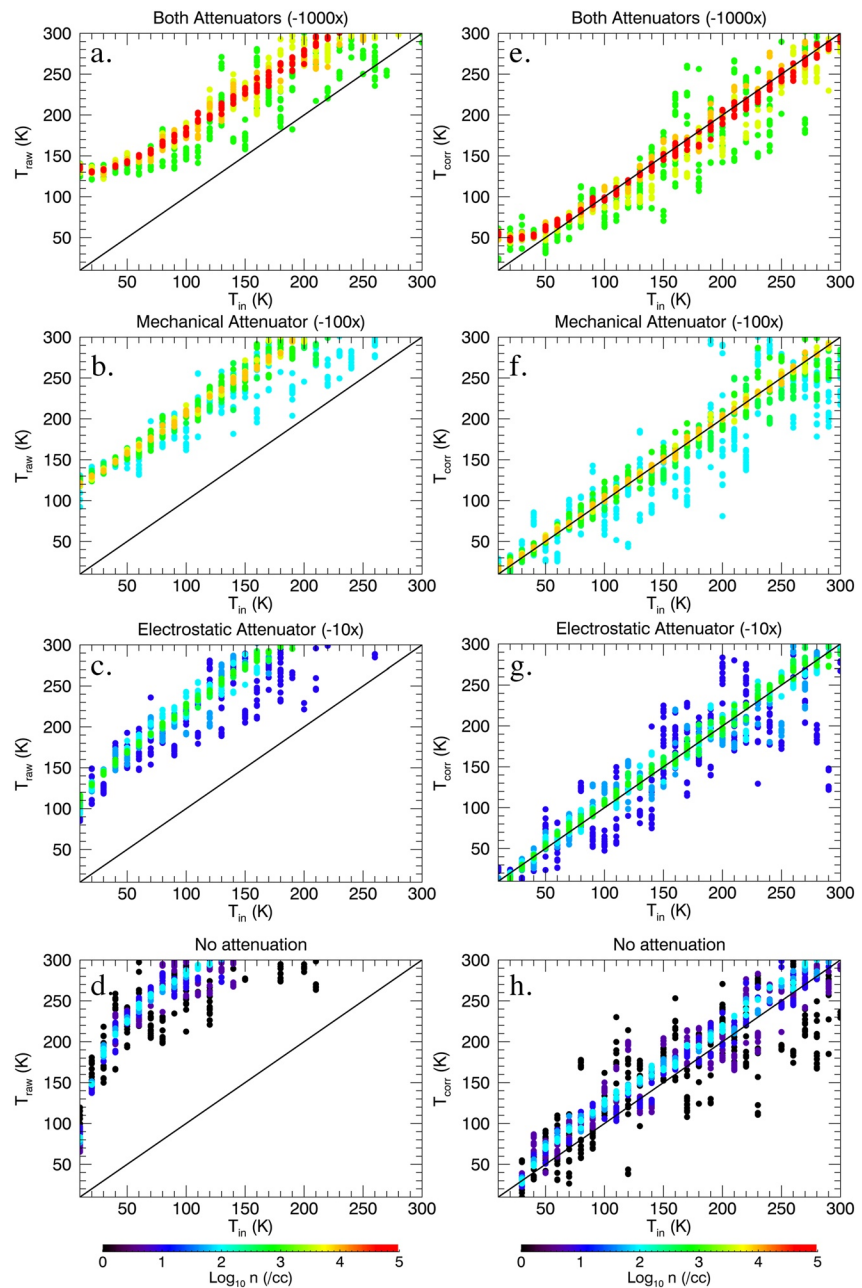
Figure 3. O_2^+ energy beamwidth temperatures, (a–d) raw and (e–h) corrected for analyzer response, as a function of the temperature T_{in} of a simulated Maxwellian distribution measured with a simulated STATIC. Color indicates the density of the simulated distribution function. Each row of figures represents a different attenuator state; the number in parentheses indicates the factor by which the ram flux is reduced. The effects of ion suppression and scattering are not included in the simulation. Ion suppression does not affect the temperature measurement; $T_{scatter}$ is zero during the passes analyzed in this work.

3. Results

Median O_2^+ temperature profiles measured during DDs 5–9, each of which occurred at different local times, are plotted in Figure 5, with upper and lower quartiles indicated by the shaded regions. Temperature measurements are binned by CO_2 density measured by the Neutral Gas and Ion Mass Spectrometer (NGIMS) (Mahaffy et al., 2015) and median values indicate the median temperature measured in each pressure bin. The largest differences between DD profiles are likely due to the different SZAs during each DD. The ephemeris data for
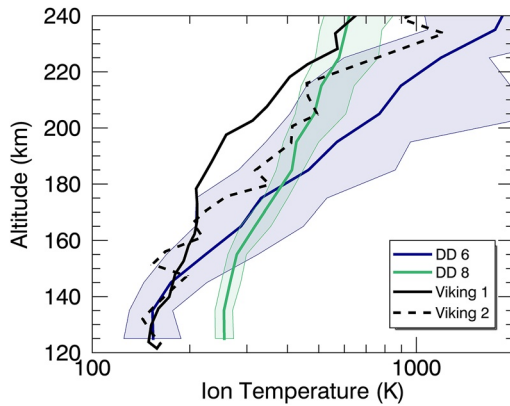
Figure 4. Median O_2^+ temperature profiles measured by STATIC during Deep Dips 6 and 8 compared to the Viking RPA ion temperatures. Shaded regions indicate upper and lower quartiles for each 10-km altitude bin.

each analyzed DD was taken in part from Stone et al. (2018) and is shown in Table 2.

We find that dayside profiles are warmer than nightside profiles below the exobase region ($\sim$170–200 km). At periapsis, the median temperature at 14:00 was 255 ± 13 K, compared to 162 ± 32 K at 01:00, where the given ranges indicate upper and lower quartiles rather than uncertainty. Dusk temperatures are warmer than dawn temperatures, which are of similar magnitude to temperatures at midnight; the difference between dawn and dusk is likely because MAVEN and the ionosphere were in darkness during the inbound orbit segments of DD 5, while DD 7 took place on the sunlit side of the terminator.

Below the exobase region, O_2^+ temperature measurements for subsequent orbits for which local solar time, latitude, and solar irradiation are similar are highly repeatable. Nightside temperatures are more variable than on the dayside. We expected higher variability on the nightside due to the patchy nature of electron impact ionization, which is a significant source of nightside ionospheric plasma (Adams et al., 2018).
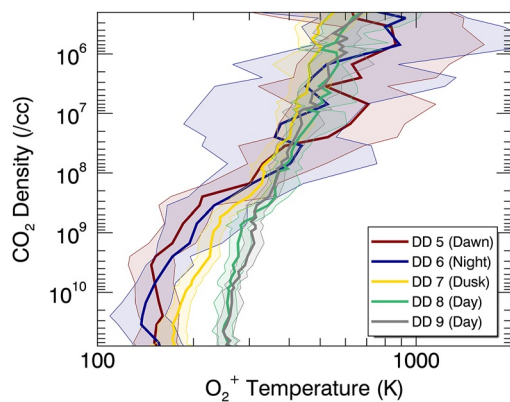
Above the exobase, acceleration and heating by electromagnetic forces and waves on some orbits lead to a wider range of observed O_2^+ temperatures at all local times. A future study will investigate the ion heating processes operating near the exobase. Some differences in DD profiles may be driven by variations in solar flux due to changing seasons; an extensive discussion of the solar EUV flux measurements during DDs can be found in Stone et al. (2018).

Interpretation of ion temperatures measured above the exobase must be handled carefully. As stated, both the angular and energy beamwidth methods assume the presence of a dominant Maxwellian core to the distribution. Above the exobase, electromagnetic forces and precipitating pickup ions can lead to the development of a suprathermal tail on the ion distribution, invalidating our assumption of a perfect Maxwellian. While the temperature calculated using our method still accurately characterizes the Maxwellian portion of the distribution, the core temperature does not accurately describe the suprathermal portion of the distribution, which may contain a significant amount of energy compared to the cold core. Temperatures calculated using the second moment (Equation 1) will always be higher than the core temperatures derived from the energy and angular beamwidths.

Figures 6 and 7 show temperature profiles for O_2^+, Ar, and electrons measured during MAVEN DDs 5–8. The Ar temperature is measured by MAVEN NGIMS using a scale-height method based on the work of Cui et al. (2009) and described by Stone et al. (2018). Though Ar is not the dominant neutral species, all neutral species have been measured to have the same temperature throughout this altitude regime, and since Ar is a noble gas, its temperature is less sensitive to instrumental effects than the CO_2 temperature (Stone et al., 2018). The electron temperature is measured by MAVEN's LPW experiment, recalibrated as described by Ergun, Andersson, Fowler, and Thaller (2021).

All temperature profiles plotted in Figures 5–7 were derived from data collected only on inbound orbit segments for two reasons. First, Ar temperatures are not available on the outbound orbit segment due to increased levels of background in NGIMS, as discussed by Stone et al. (2018). Additionally, temperatures for all populations depend on SZA, so using only measurements from the inbound orbit segment eliminates some of the variability caused by changing SZA.

Figure 5. Median O_2^+ temperature profiles measured by STATIC during the inbound orbit segments of each orbit during Deep Dips 5, 6, 7, 8, and 9, then binned by CO_2 density measured by NGIMS. Shaded regions indicate upper and lower quartiles.

Most interestingly, we find that temperature differences between ions, neutrals, and electrons persist down to the lowest altitudes sampled by MAVEN. Dayside ions are significantly hotter than the neutral atmosphere at all altitudes, while nightside ion temperatures approach neutral temperatures below the exobase, but are even hotter than dayside ions at high altitudes. Median periapsis O_2^+ temperatures are at least 15 K higher than median Ar

Table 2
MAVEN Deep Dip Periapsis Ephemeris Data

DD	Orbits	Latitude	SZA (°)	Local time (h)	L_S (°)	Crustal field
5	3,285–3,327	33.2°N	95	5.2	166.9	No
6	3,551–3,586	2.9°S	140	0.7	194.4	No
7	5,574–5,620	63.6°N	88	20.3	49.4	No
8	5,909–5,950	18.9°S	25	13.7	76.3	No
9	6,935–6,973	47.8°S	16	11.9	165.8	Yes

temperatures at all local times. At the highest CO_2 densities during DD 8, the median O_2^+ temperature is 255 ± 13 K, while the median neutral temperature is 125 ± 11 K and the median electron temperature is 294 ± 7 K. On the nightside, during DD 6, the ion and neutral temperatures drop to 162 ± 32 K and 100 ± 14 K, while the electron temperature rises to 742 ± 154 K. High temperatures in the morning (DD 5) may be associated with the morning overshoot, which was observed in electrons and ions at Earth (Evans, 1965; Redmon et al., 2012) and has been seen in electrons at Mars (Pilinski et al., 2019). The sustained temperature differences between populations, which are significant compared to the uncertainties, suggest that a fundamental piece of physics is missing from existing models of the Mars ionosphere, which assume that ion and neutral temperatures converge quickly below the exobase.

At higher altitudes, where neutral densities drop below 10^8/cc, nightside ion temperatures can approach and even exceed the electron temperature, reaching 1000s of K, while dayside temperatures remain well below 1000 K. At all local times, ion temperatures are hundreds of Kelvins higher than neutral temperatures for neutral densities lower than 10^8/cc. The convergence of ion and electron temperatures at higher altitudes is expected as the plasma transitions from collisional to magnetized (Schunk & Nagy, 2009). Discrepancies between median ion and electron temperatures at high altitudes are likely to result from the exclusion of suprathermal ions.
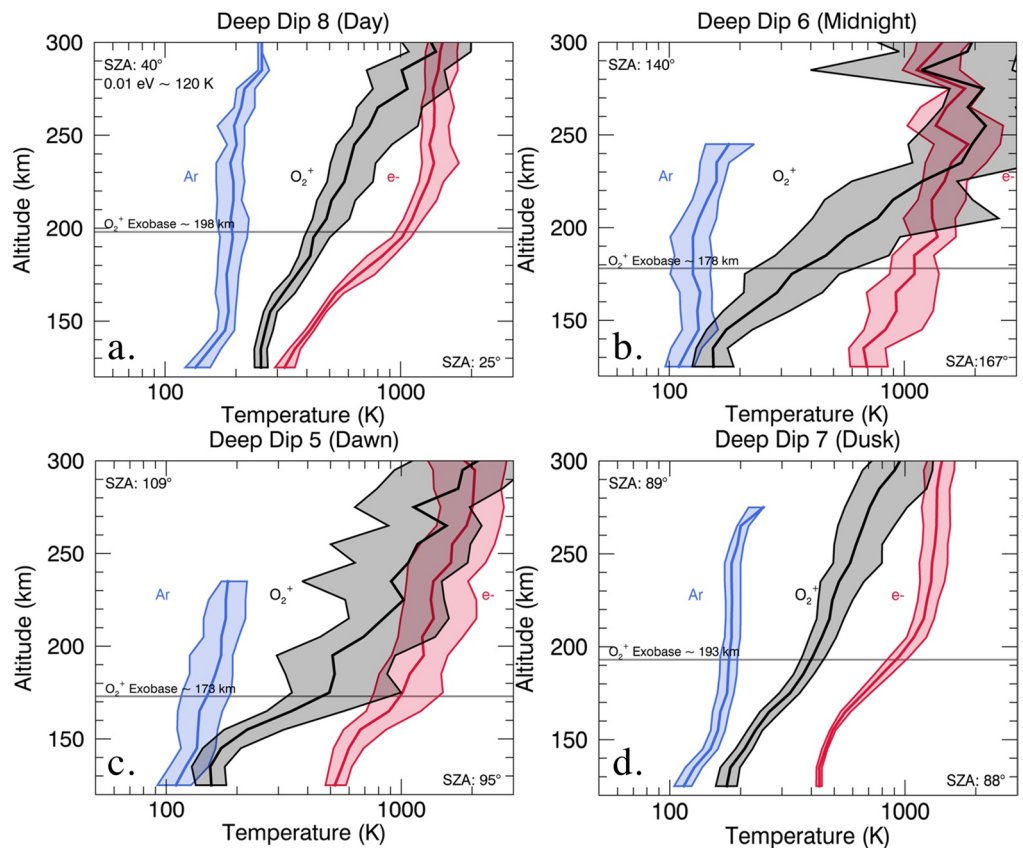
Figure 6. Median temperature profiles as a function of altitude for O_2^+, Ar, and electrons collected during (a) Deep Dip (DD) 8 at 14:00 local time, (b) DD 6 at 01:00, (c) DD 5 at 05:00, and (d) DD 7 at 20:00. O_2^+ temperatures from STATIC are shown in black, neutral Ar temperatures measured by Mars Atmosphere and Volatile EvolutioN (MAVEN) NGIMS are shown in blue, and electron temperatures from MAVEN LPW are shown in red. Shaded regions represent upper and lower quartiles. Solar zenith angles at the top and bottom of the profiles, which vary by 16° at most, are indicated on the plots. Exobase altitudes indicate where the ion scale height exceeds the mean free path between ion-neutral collisions.
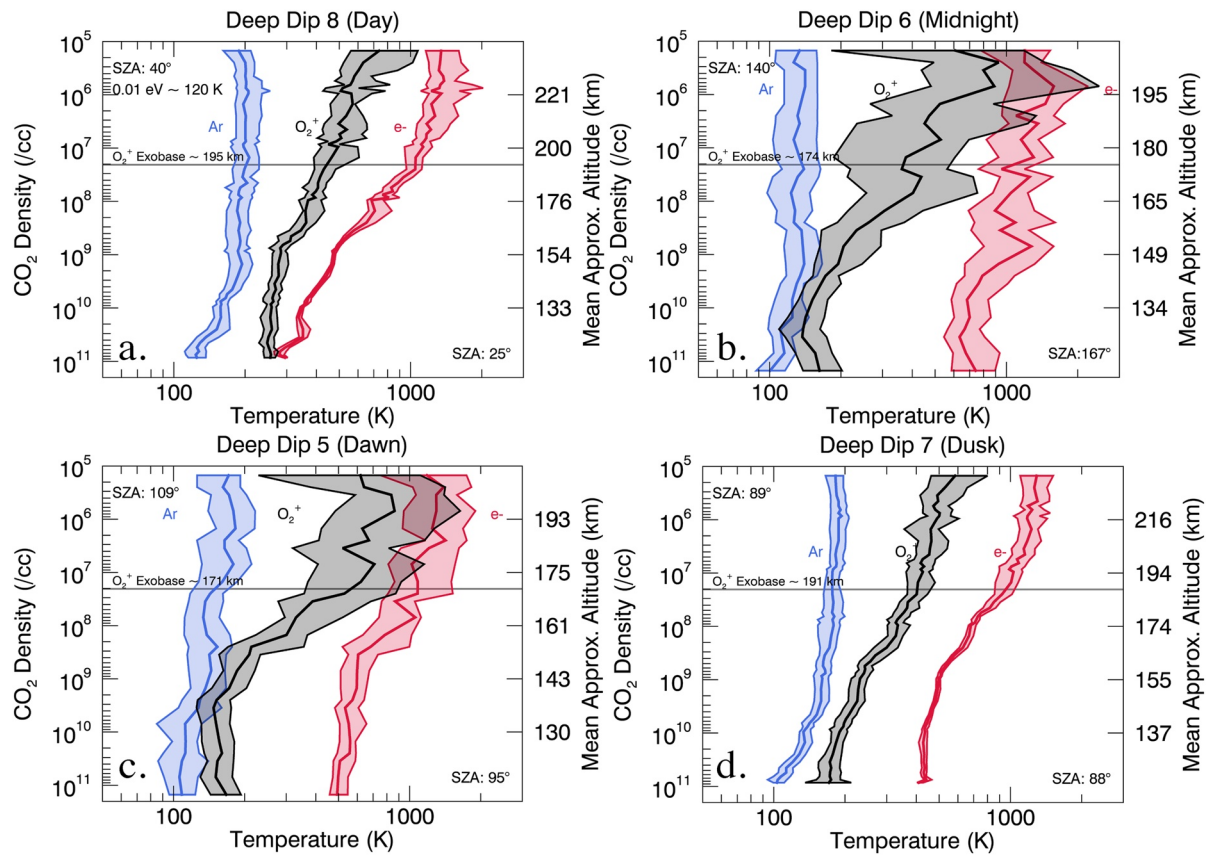
Figure 7. Median temperature profiles as a function of CO_2 density for O_2^+, Ar, and electrons collected during (a) Deep Dip (DD) 8 at 14:00 local time, (b) DD 6 at 01:00, (c) DD 5 at 05:00, and (d) DD 7 at 20:00. O_2^+ temperatures from STATIC are shown in black, neutral Ar temperatures measured by Mars Atmosphere and Volatile EvolutioN (MAVEN) NGIMS are shown in blue, and electron temperatures from MAVEN LPW are shown in red. Shaded regions represent upper and lower quartiles. Solar zenith angles at the top and bottom of the profiles, which vary by 16° at most, are indicated on the plots. Exobase altitudes indicate where the ion scale height exceeds the mean free path between ion-neutral collisions.

4. Discussion

Here we investigate the steps of ion production and thermalization in an attempt to identify processes that could energize ions at a sufficient rate to maintain the observed temperature difference between ions and neutrals. The even larger discrepancy between electron and neutral temperatures is discussed in detail by Ergun, Andersson, Fowler, Thaller, et al. (2021). We begin with photoionization, which produces radicals that participate in a network of chemical reactions. We then consider Coulomb collisions with electrons, energy transport by ions, Joule heating, and interactions with electromagnetic waves, crustal magnetic fields, or the spacecraft itself. In order to quantitatively compare the different processes, we have used a 1-D fluid model of the Mars ionosphere coupled to a kinetic suprathermal electron transport model as described by Matta et al. (2014) to calculate ion heating and cooling rates and the energy contribution due to thermal conductivity. Median ion, neutral, and electron density and temperature profiles from each DD were used as model inputs; the input temperature profiles are shown in Figure 6 and the input density profiles are shown in Figure 8. Density and temperature profiles for all species were extrapolated down to 80 km using parametric fits to the measurements, as was done by Mendillo et al. (2011) and Matta et al. (2014). The simulation results are plotted in Figure 9.

4.1. Photoionization

The first step in the formation of ionospheric O_2^+ is the photoionization of CO_2, which is rapidly converted to O_2^+ via atmospheric chemistry. During photoionization, the majority of the energy in excess of the ionization potential is carried away by the much lighter electron, while the energy delivered to the ion is usually assumed to be negligible.
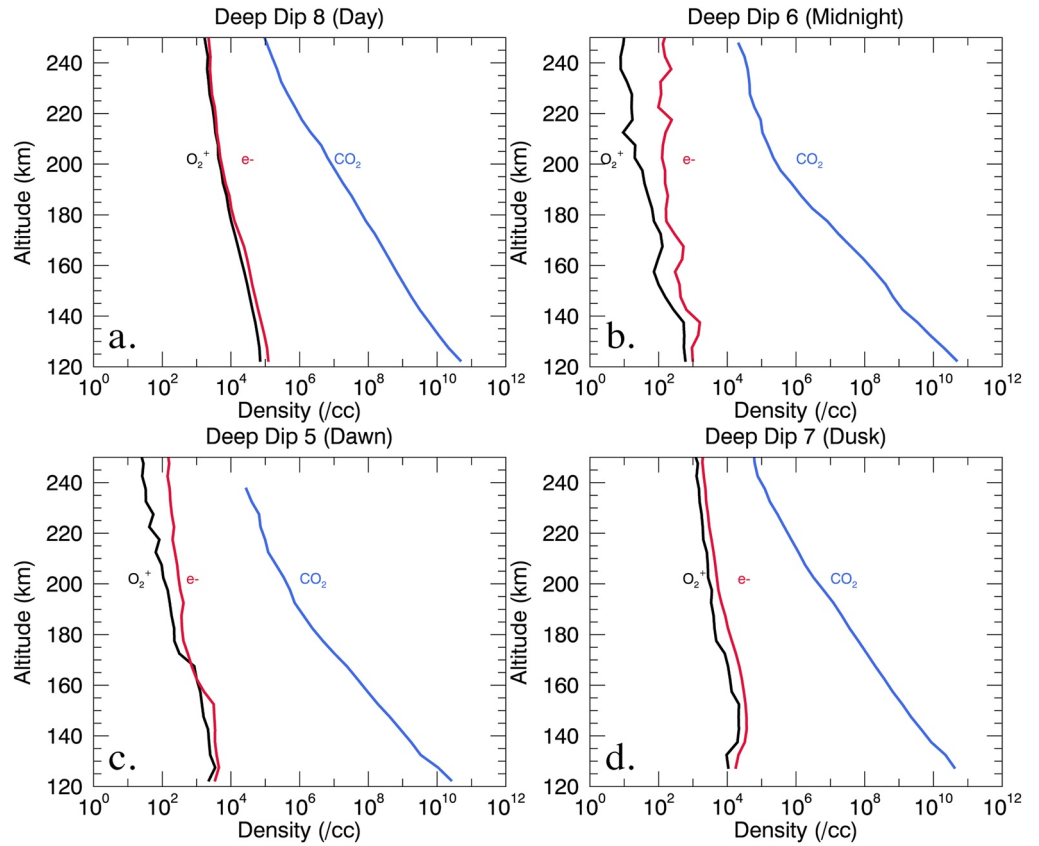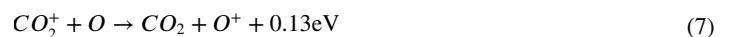
Figure 8. Median density profiles as a function of altitude for O_2^+, CO_2, and electrons collected during (a) Deep Dip (DD) 8 at 14:00 local time, (b) DD 6 at 01:00, (c) DD 5 at 05:00, and (d) DD 7 at 20:00. O_2^+ densities from STATIC are shown in black, neutral CO_2 densities measured by Mars Atmosphere and Volatile EvolutioN (MAVEN) NGIMS are shown in blue, and electron densities from MAVEN LPW are shown in red. Differences in O_2^+ and electron densities are partly due to the presence of additional ion species. Larger discrepancies may occur at high altitudes because uncertainties in electron density increase as the density decreases (Fowler et al., 2015). These differences do not significantly affect model output.

The photoelectron spectrum near the peak of the Martian ionosphere has peaks between 21 and 24 eV and at 27 eV (Fox & Dalgarno, 1979). During the production of a 27 eV photoelectron from a CO_2 gas at 125 K, momentum conservation requires that the CO_2^+ ion gain a velocity that is lower than the electron's velocity by a factor of 10^{-5}, corresponding to ~3 K of heating. Photoionization cannot provide the energy required to sustain the temperature difference between O_2^+ and neutral species, which was observed to be ~130 K during DD 8.

4.2. Atmospheric Chemistry

After photoionization, the CO_2^+ that is produced near the ionospheric peak is quickly converted into O_2^+ via a network of reactions:

$$CO_2^+ + O \rightarrow CO + O_2^+ + 1.33\text{eV} \tag{6}$$

$$CO_2^+ + O \rightarrow CO_2 + O^+ + 0.13\text{eV} \tag{7}$$

$$CO_2 + O^+ \rightarrow CO + O_2^+ + 1.2\text{eV} \tag{8}$$

No measurements of the branching ratios, which describe the fraction of the products that are produced in each excitation state, have been made for Reaction 6. However, Walter et al. (1993) measured branching ratios for Reaction 8 and found that roughly 40% of the energy released in the reaction was partitioned to internal excitation of the O_2^+ ions. In order to estimate a chemical heating rate, we therefore assume that 40% of the energy released in each reaction excites internal states of the O_2^+, and the remaining energy is divided amongst the products
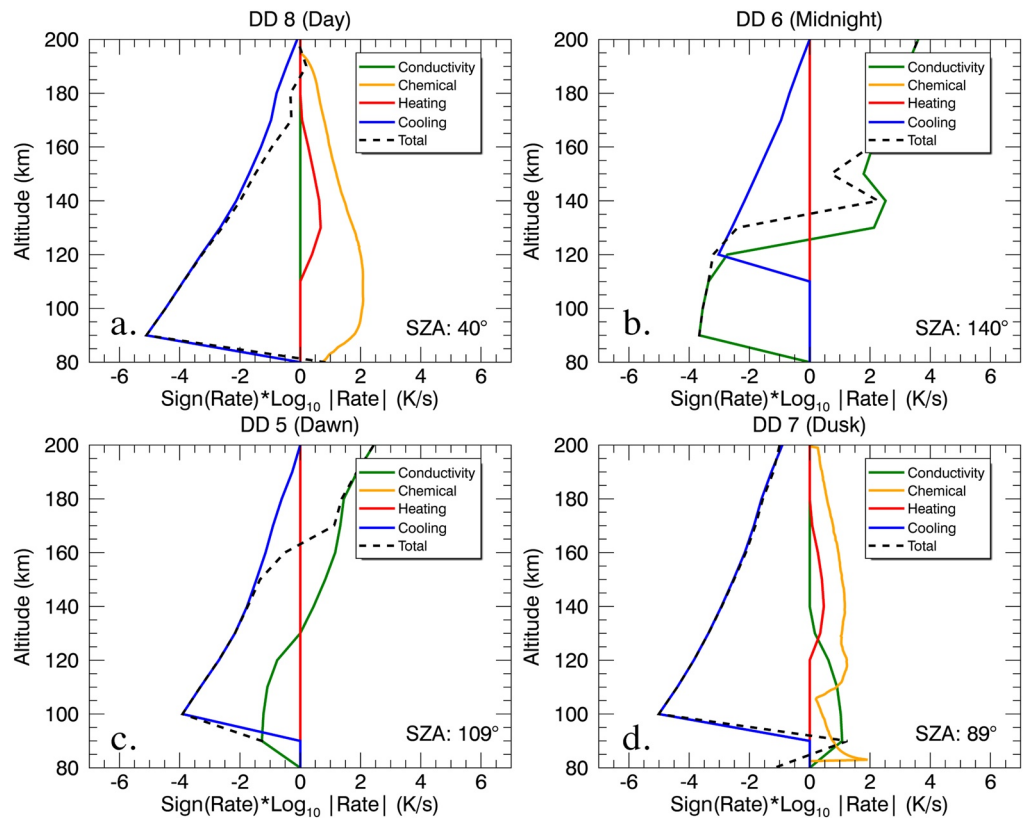
Figure 9. Heating and cooling rates for O_2^+ during DDs 5–8 assuming a single solar zenith angle as indicated on each plot. The log of each rate in K/s is plotted on the x-axis, where negative rates indicate cooling and positive rates indicate heating. Rates below 1 K/s, which would result in a negative log, were excluded from the data set. The thermal conductivity term accounts for the effects of temperature gradients, the heating rate represents the energy gained through Coulomb collisions with electrons, and the cooling rate represents the energy lost through collisions with neutrals. The conductivity, heating, and cooling terms are calculated using the Matta et al. (2014) ionosphere model. The chemical heating term represents energy deposited by atmospheric chemistry and is calculated as described in the text.

according to their mass ratio. In total, the newly produced O_2^+ ion gains a translational kinetic energy of ~0.35 eV, which will be transferred to the neutral population via collisions. If O_2^+ ions are produced faster than they can transfer this excess energy away, then the O_2^+ ions can maintain a higher temperature than the neutrals.

The chemical heating rate (orange line) in Figure 9 is not calculated by the model and was derived separately using O_2^+ production rates and electron density profiles plotted in Figures 3 and 5 of Mayyasi and Mendillo (2015), assuming that ions gain 0.35 eV per reaction. On the dayside, translational kinetic energy deposited into the O_2^+ by atmospheric chemistry is not sufficient to balance the energy lost to collisions with neutrals. On the nightside, the parametric fit to the ion temperature profile decreases with altitude between about 80 and 110 km, then starts increasing, causing thermal conductivity to dominate over collisional cooling at the lowest altitudes. The chemical heating rate drops to zero because of the lack of photoionization. Chemical heating apparently cannot explain the observed temperature differences. Even if 100% of the energy released during the reaction is assumed to be deposited as heat, with no energy partitioned to internal excitation, the chemical heating rate is orders of magnitude lower than the cooling rate and any energy gained from the chemistry is quickly transferred to the neutrals.

4.3. Coulomb Collisions With Electrons

Ions can be preferentially heated by Coulomb collisions with thermal electrons if electrons deposit energy into ions faster than the ions transfer energy into neutrals via collisions. However, the heating rate due to Coulomb collisions (red line in Figure 9) is orders of magnitude lower than the estimated cooling rates due to elastic and inelastic collisions (blue line) or thermal conduction (green line).

In addition to thermal electrons, photoelectrons may be important to the ionospheric energy balance. We investigated whether collisions with photoelectrons, which have much higher energies than the thermal electron population, could preferentially heat the ions. Schunk and Hays (1971) state that the transfer rate of energy from photoelectrons to ions is negligible. This can be explained by a small collision cross-section. Expressions for the energy loss of a test particle in a plasma (e.g., Itikawa & Aono, 1966) depend on the ratio of the velocities of the test particle and ambient particles, with the largest cross-section occurring when the ratio is of order unity. Because photoelectrons travel much faster than thermal ions, the cross-section is very small and the energy transfer is inefficient.

4.4. Energy Transport by Ions

We used the Matta et al. (2014) model to investigate whether adiabatic expansion or ion advection, which can transport heat vertically, could explain the observed ion temperatures. By setting the transport terms equal to the cooling rate, it is possible to derive plasma velocity profiles as a function of altitude. However, the resulting ion velocity profiles required to maintain the observed ion temperatures are nonphysical, approaching the speed of light near the ionospheric main peak.

4.5. Joule Heating

In the terrestrial ionosphere, electric fields push ions through the neutral gas, creating drag and heating the ions. Schunk and Nagy (2009) provide expressions to calculate ion temperatures as a function of neutral temperature and the electric and magnetic field vectors (Equations 5.35–5.37). In order to explain the temperature difference of $\sim$130 K observed at the highest CO_2 densities during DD 8, we find that a bulk differential velocity of hundreds of meters per second is required, corresponding to an electric field on the order of 1 mV/m.

At Earth, convection electric fields can be mapped downwards along magnetospheric magnetic field lines, creating powerful electric fields deep in the ionosphere. No clear candidate exists for an electric field to drive strong differential ion flows at Mars, which lacks a global magnetic field. The ambipolar electric field created by the electron pressure gradient has been estimated at the order of 1 µV/m based on MAVEN measurements in the ionosphere (Akbari et al., 2019; Xu et al., 2018). Model predictions indicate that the fields induced by the interaction with the solar wind are similarly insufficient in magnitude; Y. Dong et al. (2019) showed that the $-\vec{u} \times \vec{B}$ force will be of similar magnitude to the ambipolar field in the ionosphere, while the $\vec{J} \times \vec{B}/ne$ force will be much weaker. Neutral winds may also drive ionospheric currents. We used profiles of ionospheric conductivity and current density modeled by Lillis et al. (2019) to estimate the strength of electric fields in current systems driven by neutral winds at the order of 1 µV/m. None of these electric fields is strong enough for Joule heating to explain the temperature difference.

4.6. Localized Interactions With Crustal Magnetic Fields or Electromagnetic Waves

While Mars lacks a global magnetic field, portions of its crust are strongly magnetized, and magnetic fields in the upper atmosphere can reach thousands of nanoTeslas in magnitude (Acuña et al., 1999). Crustal fields are mainly concentrated in the Southern hemisphere, meaning that ionospheric plasma could be heated in certain geographic locations with strong crustal magnetic fields. In strong field regions, O_2^+ becomes magnetized and flows along magnetic field lines, meaning that neutral winds blowing across field lines can set up relative motion between ions and neutrals. If this were the case, then temperatures measured near crustal fields should be warmer and more variable than temperatures measured away from crustal fields. In Figure 5, we compare temperature profiles measured during DDs 8 and 9, which occurred at similar local times. The periapsis of DD 9 was located in the Southern hemisphere near the strong crustal field regions, while DD 8 was in the Northern hemisphere. We see no evidence of significantly warmer, more variable ion temperatures near crustal fields.

Electromagnetic waves have been shown as a viable heat source for ionospheric plasma by both models (Andersson et al., 2010) and MAVEN data (Fowler et al., 2017). However, all evidence to date suggests that electromagnetic waves damp and deposit their energy to the ionospheric constituents well above the exobase region, and are an unlikely sustained heating source at the ionospheric peak.
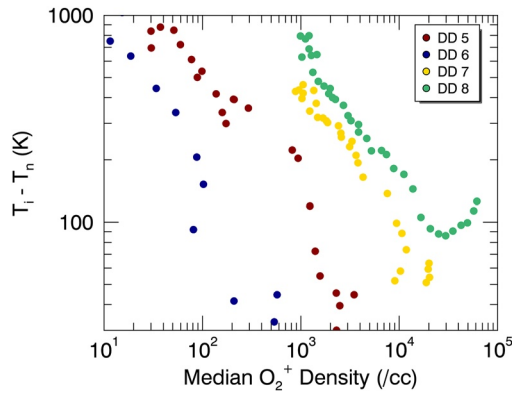
Figure 10. Median temperature discrepancy between ions and neutrals versus ion density. Considering all four Deep Dips, the temperature discrepancy is not a function of ion density, which would be expected if the discrepancy were caused by reflected ion heating.

4.7. In Situ Heating by Particles Reflected off the Spacecraft

The difficulties in measuring in situ plasma parameters due to the interaction of spacecraft with ambient plasma have been under study for decades (De-Forest, 1972; Hastings, 1995; Whipple, 1981). These issues range from the relatively simple acceleration of plasma by a charged surface, to the generation of a complex cloud of plasma surrounding the spacecraft and interacting with the environment. MAVEN's orbital velocity is about 4 km/s at periapsis, too slow to result in impact ionization of CO_2; however, it is possible that particles reflect off the spacecraft, travel back upstream and heat the ions that STATIC then measures.

The reflected ion heating rate should depend on spacecraft attitude: a larger surface area in the ram direction would reflect more particles and lead to more heating. As described in Section 2.3, we have investigated the effect of spacecraft attitude on temperature profiles during MAVEN's nominal science orbit, with periapsis at 150 km. We find no systematic difference in temperatures measured in different spacecraft orientations in the nominal orbit. It is possible that the effect only becomes significant at DD altitudes.

In addition to spacecraft attitude, the reflected ion heating rate is expected to be a function of ion density because larger temperature discrepancies were observed in the denser dayside ionosphere than on the nightside. In Figure 10, we have binned values of the difference between ion and neutral median temperatures by median ion density, which varies with the different DDs. The local minimum observed in the discrepancy profiles is expected because the neutral temperature decreases at the highest CO_2 densities. While the temperature discrepancy and ion density are generally anti-correlated, the discrepancy does not appear to be a function of ion density when all the DDs are considered together. Heating of ionospheric plasma by particles reflected off the spacecraft is therefore unlikely to explain the temperature discrepancy.

4.8. Unidentified Instrumental Errors

It is possible, but unlikely that the measured discrepancy is due to an uncorrected instrumental effect or a systematic error introduced during data calibration. NGIMS temperatures are measured to be generally in agreement with temperatures measured by the MAVEN accelerometer experiment (Zurek et al., 2015) and other measurements by accelerometers, landers, and remote sensing investigations (Stone et al., 2018). While no comparable data set exists to validate STATIC data, extensive steps have been taken by the team to identify instrumental effects that could impact ion temperatures, as described in Section 2.3. The value of T_{AC} can be adjusted to remove discrepancies between ion and neutral temperatures on any given orbit; however, applying these adjusted calibrations to other orbits produces results that are obviously incorrect, including negative temperatures. It is not possible to systematically correct the ion temperature with a single fixed algorithm to remove discrepancies with neutral temperatures on a by-orbit basis.

5. Summary and Conclusion

We have used two independent methods to calculate thermal ion temperatures at Mars for the first time since the Viking lander descents in 1976. We find that dayside profiles show little variability below the exobase region; above the exobase, electromagnetic forces and wave heating cause temperatures to vary from orbit to orbit. On the nightside, variability is more common at all altitudes due to the patchy nature of the nightside ionosphere. Our future work will use the methods described here to calculate ion temperatures for over 10,000 MAVEN orbits spanning wide ranges of latitude, local time, Mars season, and solar conditions.

Analysis of STATIC data show that ion temperatures are enhanced over neutral temperatures by typically dozens of K at periapsis, a difference that is statistically significant. Our rigorous methods for validating STATIC ion temperatures through simulations and observational procedures provide us with confidence that the derived ion temperatures are correct. Subsequent analysis has eliminated several possible mechanisms that may cause this

temperature difference, including photoionization, chemical heating, Coulomb collisions with electrons, Joule heating, energy transport by ions, heating by plasma waves or crustal fields, and heating by ions reflected off the spacecraft. The source of the energy sustaining the higher ion temperatures remains unclear.

The unexpected enhancement of ion temperatures over neutral temperatures in Mars' lower ionosphere reveals a gap in our understanding of thermalization in planetary ionospheres. The authors are not aware of any simultaneous in situ measurements of ion, neutral, and electron temperatures in the terrestrial ionosphere. A mission to measure these quantities in the terrestrial ionosphere is a logical next step in addressing the questions raised by this study.

Data Availability Statement

The data used in this paper are publicly available through NASA's Planetary Data System (https://pds-ppi.igpp.ucla.edu/search/view/?f=yes&id=pds://PPI/maven.static.c).

References

Acuña, M. H., Connerney, J. E., Ness, N. F., Lin, R. P., Mitchell, D., Carlson, C. W., et al. (1999). Global distribution of crustal magnetization discovered by the Mars Global Surveyor MAG/ER experiment. *Science*, *284*(5415), 790–793. https://doi.org/10.1126/science.284.5415.790

Adams, D., Xu, S., Mitchell, D. L., Lillis, R. L., Fillingim, M., Andersson, L., et al. (2018). Using magnetic topology to probe the sources of Mars' nightside ionosphere. *Geophysical Research Letters*, *45*(22), 12190–12197. https://doi.org/10.1029/2018GL080629

Akbari, H., Andersson, L., Peterson, W. K., Espley, J., Benna, M., & Ergun, R. (2019). Ambipolar electric field in the Martian ionosphere: MAVEN measurements. *Journal of Geophysical Research: Space Physics*, *124*(6), 4518–4524. https://doi.org/10.1029/2018JA026325

Andersson, L., Ergun, R. E., & Stewart, A. I. (2010). The combined atmospheric photochemistry and ion tracing code: Reproducing the Viking lander results and initial outflow results. *Icarus*, *206*(1), 120–129. https://doi.org/10.1016/j.icarus.2009.07.009

Barabash, S., Lundin, R., Andersson, H., Brinkfeldt, K., Grigoriev, A., Gunell, H., et al. (2006). The Analyzer of Space Plasmas and EneRgetic Atoms (ASPERA-3) for the Mars Express mission. *Space Science Reviews*, *126*(1–4), 113–164. https://doi.org/10.1007/s11214-006-9124-8

Bougher, S. W., Pawlowski, D., Bell, J. M., Nelli, S., McDunn, T., Murphy, J. R., et al. (2015). Mars Global Ionosphere-Thermosphere Model: Solar cycle, seasonal, and diurnal variations of the Mars upper atmosphere. *Journal of Geophysical Research: Planets*, *120*, 311–342. https://doi.org/10.1002/2014JE004715

Chassefière, E., & Leblanc, F. (2004). Mars atmospheric escape and evolution; interaction with the solar wind. *Planetary and Space Science*, *52*(11), 1039–1058. https://doi.org/10.1016/j.pss.2004.07.002

Chen, R. H., Cravens, T. E., & Nagy, A. F. (1978). The Martian ionosphere in light of the Viking observations. *Journal of Geophysical Research*, *83*(A8), 3871–3876. https://doi.org/10.1029/ja083ia08p03871

Cui, J., Yelle, R. V., Vuitton, V., Waite, J. H., Kasprzak, W. T., Gell, D. A., et al. (2009). Analysis of Titan's neutral upper atmosphere from Cassini Ion Neutral Mass Spectrometer measurements. *Icarus*, *200*(2), 581–615. https://doi.org/10.1016/j.icarus.2008.12.005

DeForest, S. E. (1972). Spacecraft charging at synchronous orbit. *Journal of Geophysical Research*, *77*(4), 651–659. https://doi.org/10.1029/ja077i004p00651

Dong, C., Bougher, S. W., Ma, Y., Toth, G., Nagy, A. F., & Najib, D. (2014). Solar wind interaction with Mars upper atmosphere: Results from the one-way coupling between the multifluid MHD model and the MTGCM model. *Geophysical Research Letters*, *41*(8), 2708–2715. https://doi.org/10.1002/2014GL059515

Dong, Y., Brain, D., Jarvinen, R., Poppe, A. R., Egan, H. L. & Fang, X. Localized hybrid simulation of Martian crustal magnetic cusp regions. 2019 EPSC-DPS Joint Meeting, Geneva, Switzerland.

Ergun, R. E., Andersson, L. A., Fowler, C. M., & Thaller, S. A. (2021). Kinetic modeling of Langmuir probes in space and application to the MAVEN Langmuir probe and waves instrument. *Journal of Geophysical Research: Space Physics*, *126*(3), 1–17. https://doi.org/10.1029/2020JA028956

Ergun, R. E., Andersson, L. A., Fowler, C. M., Thaller, S. A., & Yelle, R. V. (2021). In-situ measurements of electron temperature and density in Mars' dayside ionosphere. *Geophysical Research Letters*, *48*(14), 1–10. https://doi.org/10.1029/2021GL093623

Ergun, R. E., Morooka, M. W., Andersson, L. A., Fowler, C. M., Delory, G. T., Andrews, D. J., et al. (2015). Dayside electron temperature and density profiles at Mars: First results from the MAVEN Langmuir probe and waves instrument. *Geophysical Research Letters*, *42*(21), 8846–8853. https://doi.org/10.1002/2015GL065280

Evans, J. V. (1965). Cause of the midlatitude winter night increase in f 0 F 2. *Journal of Geophysical Research*, *70*(17), 4331–4345. https://doi.org/10.1029/jz070i017p04331

Fallows, K., Withers, P., & Matta, M. (2015a). An observational study of the influence of solar zenith angle on properties of the M1 layer of the Mars ionosphere. *Journal of Geophysical Research: Space Physics*, *120*(2), 1299–1310. https://doi.org/10.1002/2014JA020750

Fallows, K., Withers, P., & Matta, M. (2015b). An observational study of the influence of solar zenith angle on properties of the M1 layer of the Mars ionosphere. *Journal of Geophysical Research: Space Physics*, *120*(2), 1299–1310. https://doi.org/10.1002/2014JA020750

Fowler, C. M., Andersson, L., Ergun, R. E., Morooka, M., Delory, G., Andrews, D. J., et al. (2015). The first in situ electron temperature and density measurements of the Martian nightside ionosphere. *Geophysical Research Letters*, *42*(21), 8854–8861. https://doi.org/10.1002/2015GL065267

Fowler, C. M., Andersson, L., Halekas, J., Espley, J. R., Mazelle, C., Coughlin, E. R., et al. (2017). Electric and magnetic variations in the near-Mars environment. *Journal of Geophysical Research: Space Physics*, *122*(8), 8536–8559. https://doi.org/10.1002/2016JA023411

Fox, J. L. (2015). The chemistry of protonated species in the martian ionosphere. *Icarus*, *252*, 366–392. https://doi.org/10.1016/j.icarus.2015.01.010

Fox, J. L., Brannon, J. F., & Porter, H. (1993). Upper limits to the nightside ionosphere of Mars. *Geophysical Research Letters*, *20*(13), 1391–1394. https://doi.org/10.1029/93gl01349

Fox, J. L., & Dalgarno, A. (1979). Ionization, luminosity, and heating of the upper atmosphere of Mars. *Journal of Geophysical Research*, *84*(A12), 7315–7333. https://doi.org/10.1029/ja084ia12p07315

Girazian, Z., Mahaffy, P., Lillis, R. J., Benna, M., Elrod, M., Fowler, C. M., & Mitchell, D. L. (2017). Ion densities in the nightside ionosphere of Mars: Effects of electron impact ionization. *Geophysical Research Letters*, *44*(22), 11248–11256. https://doi.org/10.1002/2017GL075431

González-Galindo, F., Eusebio, D., Němec, F., Peter, K., Kopf, A., Tellmann, S., & Paetzold, M. (2021). Seasonal and geographical variability of the Martian ionosphere from Mars express observations. *Journal of Geophysical Research: Planets*, *126*(2), 1–15. https://doi.org/10.1029/2020JE006661

Haider, S. A., Mahajan, K. K., & Kallio, E. (2011). Mars ionosphere: A review of experimental results and modeling studies. *Reviews of Geophysics*, *49*(4), 1–37. https://doi.org/10.1029/2011RG000357

Hanson, W. B., Sanatani, S., & Zuccaro, D. R. (1977). The Martian ionosphere as observed by the Viking retarding potential analyzers. *Journal of Geophysical Research*, *82*(28), 4351–4363. https://doi.org/10.1029/js082i028p04351

Hastings, D. E. (1995). A review of plasma interactions with spacecraft in low Earth orbit. *Journal of Geophysical Research*, *100*(A8), 14457. https://doi.org/10.1029/94ja03358

Itikawa, Y., & Aono, O. (1966). Energy change of a charged particle moving in a plasma. *Physics of Fluids*, *9*(6), 1259–1261. https://doi.org/10.1063/1.1761835

Jakosky, B. M., Brain, D., Chaffin, M., Curry, S., Deighan, J., Grebowsky, J., et al. (2018). Loss of the Martian atmosphere to space: Present-day loss rates determined from MAVEN observations and integrated loss through time. *Icarus*, *315*, 146–157. https://doi.org/10.1016/j.icarus.2018.05.030

Jakosky, B. M., Lin, R. P., Grebowsky, J. M., Luhmann, J. G., Mitchell, D. F., Beutelschies, G., et al. (2015). The Mars Atmosphere and Volatile EvolutioN (MAVEN) mission. *Space Science Reviews*, *195*(1–4), 3–48. https://doi.org/10.1007/s11214-015-0139-x

Lillis, R. J., Fillingim, M. O., & Brain, D. A. (2011). Three-dimensional structure of the Martian nightside ionosphere: Predicted rates of impact ionization from Mars Global Surveyor magnetometer and electron reflectometer measurements of precipitating electrons. *Journal of Geophysical Research*, *116*(A12), A12317. https://doi.org/10.1029/2011JA016982

Lillis, R. J., Fillingim, M. O., Ma, Y., Gonzalez-Galindo, F., Forget, F., Johnson, C. L., et al. (2019). Modeling wind-driven ionospheric dynamo currents at Mars: Expectations for inSight magnetic field measurements. *Geophysical Research Letters*, *46*(10), 5083–5091. https://doi.org/10.1029/2019GL082536

Ma, Y. J., Dong, C. F., Toth, G., van der Holst, B., Nagy, A. F., Russell, C. T., et al. (2019). Importance of ambipolar electric field in driving ion loss from Mars: Results from a multifluid MHD model with the electron pressure equation included. *Journal of Geophysical Research: Space Physics*, *124*(11), 9040–9057. https://doi.org/10.1029/2019JA027091

Mahaffy, P. R., Benna, M., King, T., Harpold, D. N., Arvey, R., Barciniak, M., et al. (2015). The neutral gas and ion mass spectrometer on the Mars atmosphere and volatile evolution mission. *Space Science Reviews*, *195*(1–4), 49–73. https://doi.org/10.1007/s11214-014-0091-1

Matta, M., Galand, M., Moore, L., Mendillo, M., & Withers, P. (2014). Numerical simulations of ion and electron temperatures in the ionosphere of Mars: Multiple ions and diurnal variations. *Icarus*, *227*, 78–88. https://doi.org/10.1016/j.icarus.2013.09.006

Mayyasi, M., & Mendillo, M. (2015). Why the Viking descent probes found only one ionospheric layer at Mars. *Geophysical Research Letters*, *42*(18), 7359–7365. https://doi.org/10.1002/2015GL065575

McElroy, M. B. (1972). Mars: An evolving atmosphere. *Science*, *175*(4020), 443–445. https://doi.org/10.1126/science.175.4020.443

McFadden, J. P., Kortmann, O., Curtis, D., Dalton, G., Johnson, G., Abiad, R., et al. (2015). MAVEN suprathermal and thermal ion composition (STATIC) instrument. *Space Science Reviews*, *195*(1–4), 199–256. https://doi.org/10.1007/s11214-015-0175-6

Mendillo, M., Lollo, A., Withers, P., Matta, M., Pätzold, M., & Tellmann, S. (2011). Modeling Mars' ionosphere with constraints from same-day observations by Mars Global Surveyor and Mars Express. *Journal of Geophysical Research*, *116*(A11), A11303. https://doi.org/10.1029/2011JA016865

Pilinski, M., Andersson, L., Fowler, C., Peterson, W. K., Thiemann, E., & Elrod, M. K. (2019). Electron temperature response to solar forcing in the low-latitude Martian ionosphere. *Journal of Geophysical Research: Plan*, *124*(11), 3082–3094. https://doi.org/10.1029/2019JE006090

Redmon, R. J., Peterson, W. K., Andersson, L., & Richards, P. G. (2012). Dawnward shift of the dayside O^+ outflow distribution: The importance of field line history in O^+ escape from the ionosphere. *Journal of Geophysical Research*, *117*(12), A12222. https://doi.org/10.1029/2012JA018145

Rohrbaugh, R. P., Nisbet, J. S., Bleuler, E., & Herman, J. R. (1979). The effect of energetically produced O_2^+ on the ion temperatures of the Martian thermosphere. *Journal of Geophysical Research*, *84*(9), 3327–3338. https://doi.org/10.1029/ja084ia07p03327

Schunk, R. W., & Hays, P. B. (1971). Photoelectron energy losses to thermal electrons. *Planetary and Space Science*, *19*(1), 113–117. https://doi.org/10.1016/0032-0633(71)90071-7

Schunk, R. W., & Nagy, A. F. (2009). *Ionospheres* (In J. T. Houghton, M. J. Rycroft, & A. J. Dessler (Eds.)), (2nd ed.). Cambridge University Press.

Stone, S. W., Yelle, R. V., Benna, M., Elrod, M. K., & Mahaffy, P. R. (2018). Thermal structure of the Martian upper atmosphere from MAVEN NGIMS. *Journal of Geophysical Research: Planets*, *123*(11), 2842–2867. https://doi.org/10.1029/2018JE005559

Thiemann, E. M., Chamberlin, P. C., Eparvier, F. G., Templeman, B., Woods, T. N., Bougher, S. W., & Jakosky, B. M. (2017). The MAVEN EUVM model of solar spectral irradiance variability at Mars: Algorithms and results. *Journal of Geophysical Research: Space Physics*, *122*(3), 2748–2767. https://doi.org/10.1002/2016JA023512

Walter, C. W., Cosby, P. C., & Peterson, J. R. (1993). Rovibrational product distributions of O_2^+ from the reaction of $O^+(4S)$ with CO_2. *The Journal of Chemical Physics*, *98*(4), 2860–2871. https://doi.org/10.1063/1.465072

Whipple, E. C. (1981). Potentials of surfaces in space. *Reports on Progress in Physics*, *44*(11), 1197–1250. https://doi.org/10.1088/0034-4885/44/11/002

Withers, P. (2009). A review of observed variability in the dayside ionosphere of Mars. *Advances in Space Research*, *44*(3), 277–307. https://doi.org/10.1016/j.asr.2009.04.027

Xu, S., Mitchell, D. L., McFadden, J. P., Collinson, G., Harada, Y., Lillis, R., et al. (2018). Field-aligned potentials at Mars from MAVEN observations. *Geophysical Research Letters*, *45*(19), 10119–10127. https://doi.org/10.1029/2018GL080136

Zurek, R. W., Tolson, R. H., Baird, D., Johnson, M. Z., & Bougher, S. W. (2015). Application of MAVEN accelerometer and attitude control data to Mars atmospheric characterization. *Space Science Reviews*, *195*(1–4), 303–317. https://doi.org/10.1007/s11214-014-0095-x